

**CO₂ electrochemical reduction at thiolate-modified Au electrodes**

Journal:	<i>Catalysis Science & Technology</i>
Manuscript ID	CY-ART-03-2019-000506.R1
Article Type:	Paper
Date Submitted by the Author:	22-Apr-2019
Complete List of Authors:	Fang, Yuxin; Louisiana State University, Cain Department of Chemical Engineering Cheng, Xun; Louisiana State University, Cain Department of Chemical Engineering Flake, John; Louisiana State University, Cain Department of Chemical Engineering Xu, Ye; Louisiana State University, Cain Department of Chemical Engineering

CO₂ electrochemical reduction at thiolate- modified bulk Au electrodes

Yuxin Fang, Xun Cheng, John C. Flake, and Ye Xu**

Cain Department of Chemical Engineering, Louisiana State University,

Baton Rouge, LA 70803, USA

Abstract

Electrochemical reduction provides an opportunity to convert atmospheric CO₂ to fuels or chemicals using renewable energy. In this work, we demonstrate unexpected influence on the catalytic activity and selectivity of the electrochemical CO₂ reduction reaction (CO₂RR) through the functionalization of Au with thiols. 2-Phenylethanethiol modified Au electrodes (2-PET-Au) show up to a 2-fold enhancement in both Faradaic efficiency and current density for CO evolution, between -0.6 and -0.9 V vs. the reversible hydrogen electrode. Functionalization with 2-mercaptopropionic acid, which has a readily ionized carboxylate group, leads to hydrogen evolution with up to 100% Faradaic efficiency at the expense of CO evolution. Remarkably, the adsorption of certain thiols on Au did not have a negative impact on the total current density compared to blank Au. We present evidence that it is due to ligand-induced reconstruction of Au surfaces resulting in the creation of structurally and chemically modified local reaction environments. Thus a thiol species such as 2-PET, which does not contain any nitrogen-based heterocycle with a charge transfer center, can induce the formation of active sites on Au that are electrochemically active toward CO₂RR within the range of electrode potential that most of the ligand concentration remains stable on Au. Our findings suggest a simple, effective, and tunable way to modify the activity and selectivity of Au electrodes.

1. Introduction

The ability of nature to selectively reduce CO_2 using sunlight and water is a truly exquisite process. If mankind is to develop processes to produce fuels, chemicals, and materials from these basic ingredients using renewable energy, the overall efficiency, yields, and selectivity of electroreduction reactions must be substantially improved. In electrochemical routes, a fundamental challenge is the fact that the formal potentials for the CO_2 reduction reaction (CO_2RR) forming various products (e.g. CO , CH_3OH , HCOOH) occur close to that of the hydrogen evolution reaction (HER) at 0 V vs. the standard hydrogen potential (denoted as V_{SHE} below).¹ This effectively causes most conventional electrocatalysts to generate large amounts of H_2 relative to desirable products such as hydrocarbons. In contrast, carbon monoxide dehydrogenase (CODH)² enzymes such as carboxydotherrmus hydrogenoformans^{3, 4} and carboxidovorans³ can reversibly reduce CO_2 to CO at ambient conditions, albeit at slow rates. The active site of CODH consists of a Fe_3S_4 cluster bonded to a Ni-Fe moiety, and the Ni and Fe atoms are anchored by cysteine ligands. If we can understand and leverage the function of ligands on conventional electrodes, it may be possible to develop new electrocatalysts to effectively convert CO_2 into high energy density fuels in a carbon-neutral process.

Previously, Hori et al. investigated the catalytic activity of many metal electrodes for CO_2 reduction. Au was reported to produce CO selectively in a 0.5 M KHCO_3 solution giving a Faradaic efficiency (FE) up to 91% at -1.1 V vs. the normal hydrogen electrode (NHE) and a partial current density of 3.7 mA/cm^2 . The onset potential for CO formation was -0.8 V vs. the standard hydrogen electrode (SHE).⁵⁻⁷ Ito et al. studied gold electrodes in a series of phosphate buffer solutions. By tuning the pH of the electrolyte from 2.5 to 6.8, the FE of CO formation varied from 30% to 60% with hydrocarbons produced at the more negative potentials.⁸ In an

attempt to overcome the constraint of high overpotential and low product selectivity, the use of electrodes based on nano-sized Au was considered in several studies. Kauffman et al. synthesized thiolate-stabilized Au₂₅ nanoclusters, which catalyzed the conversion of CO₂ to CO with nearly 100% FE at -1 V vs. the reversible hydrogen electrode (RHE) and a partial current density of 15 mA/cm² in 0.1 M KHCO₃, with the onset potential promoted to -0.19 V_{RHE}.⁹ Zhu et al. evaluated monodisperse Au nanoparticles (4-10 nm in diameter) in 0.5 M KHCO₃ and obtained a maximum 90% FE at -0.67 V_{RHE}. Their theoretical calculations suggested that the edge sites on the Au nanoparticles favor CO evolution over HER by stabilizing the key COOH intermediate, while corner sites favor HER over CO₂RR.¹⁰ Inspired by the finding, they further synthesized ultrathin Au nanowires, which featured a high fraction of exterior sites as edge sites, and obtain a maximum FE for CO evolution of 94% at -0.35 V_{RHE} in 0.5 M KHCO₃.¹¹ Significant size-dependent activity was also noted by Mistry et al. for 1.1-7.7 nm Au nanoparticles. Those authors reported that the FE for H₂ increased and that for CO decreased with decreasing particle size at -1.2 V_{RHE}.¹²

In addition to optimizing the size and composition of metal electrocatalysts,^{9, 13, 14} the use of molecular redox mediators represents another promising approach. Seshadri et al. reported that pyridinium ions reduced CO₂ to methanol with up to 30% FE on Pt electrodes.¹⁵ Pyridinium was proposed to function as a one-electron shuttle between the metal and CO₂.^{16, 17} Cole et al. further showed that the basicity and steric effects of substituent groups on pyridinium also correlated with the enhanced Faradaic yield of methanol in CO₂ reduction.¹⁶ Homogeneous catalysts such as Re(bipy)(CO)₃Cl and pterins supported on glassy carbon have also been reported as active catalysts for CO₂ reduction. Re(bipy)(CO)₃Cl selectively reduces CO₂ to CO, while pterins are capable of reducing CO₂ and formic acid to methanol without any metal, albeit at very low

yields.^{18, 19} Although the role of the molecular complexes in these reactions remains to be elucidated, the ligand effect is reminiscent of nature's use of ligands to achieve CO₂ reduction in photosynthesis.

We hypothesize that ligands can be used to enhance or steer electrochemical activities in CO₂RR for solid electrodes as well as for molecular clusters. Herein we present how two thiol ligands containing no nitrogen-based heterocycle alter the activity and selectivity of electrochemical CO₂RR. Unexpectedly, Au electrodes modified with 2-phenylethanethiol (C₆H₅(CH₂)₂SH, abbreviated henceforth as 2-PET; Fig. 1a) exhibit increased FE and partial current density for CO formation, whereas Au electrodes modified with 2-mercaptopropanoic acid (or thiolactic acid, CH₃CHSHCOOH, abbreviated henceforth as 2-MPA; Fig. 1b) is capable of promoting HER to nearly 100% FE at the expense of CO₂RR. The total current densities on the ligand-modified electrodes are either comparable to or higher than that on blank Au, evidencing little poisoning effect by the thiols.

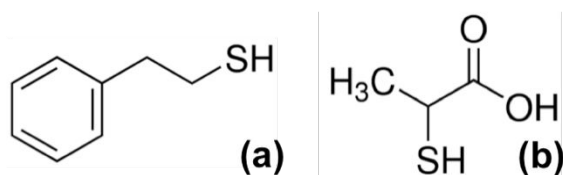


Fig. 1 Schematic of the two thiol species used to functionalize Au electrodes in this study: (a) 2-phenylethanethiol (C₆H₅(CH₂)₂SH); (b) 2-mercaptopropanoic acid (CH₃CHSHCOOH).

These two ligands belong to a large class of organothiol compounds, which are known for their tendency to self-assemble into stable monolayers (“SAMs”) on Au and other metals and have been used to functionalize solid surfaces with different chemical groups.^{1, 20-22} S-Au bonding has been confirmed by XPS,^{23, 24} and low barriers (0.3 ~ 0.4 eV) for the dissociation of the thiolic H have been shown by DFT,^{25, 26} both of which suggest dissociative adsorption of thiols as thiolates

at ambient conditions. Scanning tunneling microscopy (STM) studies have documented that the morphology of Au surfaces undergo significant changes at ambient or sub-ambient temperature with the chemisorption of many thiols, including alkyl- and phenylalkyl-thiols^{22, 27-32} and mercaptopropionic acids,³¹⁻³⁷ via formation of pits and vacancies that are predominantly monoatomic deep and develop on the order on minutes. However, the effect of the morphological changes on the chemical reactivity of Au surfaces is not understood. It has been shown conclusively that SAMs of thiols contain Au adatoms removed from the surface.³⁸⁻⁴⁰ The current structural models for SAMs on Au are based on the so-called “staple” motif (with a chemical formula of $(RS)_2Au$):^{20, 38, 40} Such dithiolate-Au complexes form various ordered phases of up to 1/3 ML (coverage based on the ratio of the number of S atoms to that of surface Au atoms) on flat terraces, although what adsorbs on defect sites is not well resolved.

Therefore we rationalize the modified CO₂RR behavior in terms of thiolate-induced surface reconstruction of Au, as illustrated in Fig. 2. The reconstruction process occurs *prior to* the electrochemical experiments, starting with the submersion of an Au foil in an ethanolic thiol solution and continuing as the Au foil is dried and later placed in a thiol-less CO₂ electrolysis solution. It proceeds as follows: A thiolate molecule (RS) extracts an Au atom out of an Au(111) surface, forming a monothiolate-Au complex (RSAu) and leaving behind a Au vacancy (V_{Au}). As this process repeats itself, V_{Au} 's coalesce into new extended defect sites while a steady supply of RSAu is generated. RSAu may further decompose into dithiolate-Au complexes ($(RS)_2Au$) by ejecting half the amount of Au adatoms, which coalesce into additional defect sites. Available defect sites then become occupied by either RS or $(RS)_2Au$ species. The net result is the conversion of Au terraces into defects decorated and stabilized by thiolate species according to

the following (unbalanced) overall reaction. Here ejected Au atoms and Au vacancies are counted together as new defect sites (\ominus):

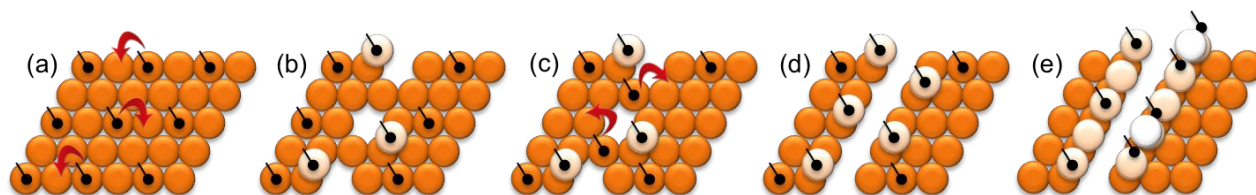
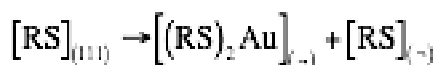


Fig. 2 Schematic illustrating a reconstruction process on Au(111): (a) thiolates (RS) cover Au(111); (b) thiolates create point vacancies by extracting Au atoms out of the surface forming monothiolate-Au complexes (RSAu); (c) the process repeats itself and more Au atoms are extracted; (d) Au vacancies coalesce into new defect sites; (e) RS and dithiolate-Au complexes ((RS)₂Au) occupy the new defect sites. Large spheres represent Au atoms (different shading denotes different layers); black dots with tails denote ligands.

Consistent on this view, we present density functional theory (DFT) calculations showing that certain thiolated Au defect sites are capable of turning over CO₂ reduction in the intermediate potential range owing to a combination of local structural and electrostatic factors, supporting the identification of such sites as the active sites for CO₂RR in the presence of thiolates. Primarily Au(111) and Au(211) facets are used as models to represent terrace and defect sites respectively, with a combination of ligands and key reaction intermediates adsorbed at medium to high coverage. While a sufficiently negative potential would undoubtedly cause most, if not all, thiol ligands to desorb, our findings suggest that intriguing and potentially tunable modification of electrocatalytic behavior may be obtained by targeted thiol modification when CO₂ electrolysis is carried out at an intermediate potential positive of ca. -1 V_{RHE}.

2. Experimental

2.1 Electrode preparation and characterization

Blank polycrystalline Au foil electrodes (99.99%, MTI Corp.) were rinsed with deionized water (Mega Pure system) and used as working electrodes. Functionalized electrodes were prepared as follows: DI water-rinsed Au foils were immersed in a 20 mM ethanolic solution of 2-phenylethanethiol (Sigma-Aldrich, 98%) or 2-mercaptopropionic acid (Sigma-Aldrich, 95%) for 10 minutes. The thiol-functionalized electrodes were then rinsed with copious amounts of ethanol (Pharmco-Aaper, ACS) after being taken out of the solutions to remove non-chemisorbed species such as un-dissociated thiols.

Attenuated total reflectance infrared (ATR-IR) spectra of the functionalized gold electrodes were taken using a smart-ITR assembled Nicolet 6700 FTIR spectrometer with a nitrogen-cooled narrow-band MCT detector. Each Au sample (blank or functionalized) was mounted on the sampling stage where the diamond crystal was located at the center, and the sample was fixed with the high-pressure clamp from the top. For each ligand-modified electrode, one spectrum was taken in the freshly prepared state. The electrodes then underwent chronoamperometry in the same two-compartment electrochemical cell at various controlled potentials down to $-1.1 V_{\text{RHE}}$, which was the most negative potential applied in CO_2 electrolysis in this study. Spectra were taken again after the system was held at each potential for 15 minutes. The spectra were recorded at a resolution of 0.5 cm^{-1} and 256 scans.

2.2 Electrochemical methods

Electrolysis of CO_2 was carried out using a three-electrode cell in a two-compartment glass reactor separated by Nafion membrane (FuelCellsEtc) to prevent the products from being re-

oxidized. The potential of the cathode was measured with respect to an Ag/AgCl (saturated with 3 M NaCl) reference electrode (BASi, RE-5B) by a PAR 263A potentiostat/galvanostat. The Pt wire in the anode compartment served as the counter electrode. CO₂ was bubbled continuously into a 0.1 M KHCO₃ (Sigma-Aldrich, ACS reagent, in Mega-Pure water) supporting electrolyte in the electrochemical cell at a flow rate of 40 ml/min and a pressure of 1 atm while the potential was stepped to a desired potential and held at it for 15 minutes. At the 15 minutes, the gas products (CO and H₂) in the effluent of the electrolysis were auto-sampled by the gas chromatograph (SHIMADZ, GC 2014) with HP-Plot U column (Agilent Technologies) that was equipped with FID and TCD detectors, and the concentrations of individual gases were analyzed.

2.3 Computational methods

All periodic DFT calculations reported in this work were performed in the generalized gradient approximation (GGA-RPBE exchange-correlation functional⁴¹) using the Vienna Ab initio Simulation Package (VASP).⁴² The core electrons were described using the Projector Augmented Wave (PAW) method.⁴³ The equilibrium lattice constant for Au was determined to be 4.198 Å, in good agreement with the experimental value (4.08 Å).⁴⁴ The valence electrons were expanded in Kohn-Sham one-electron orbitals up to 400 eV.

The Au(111) and Au(100) surfaces were modeled with slabs that had a (2×2) or (3×3) surface unit cell with 4 layers of Au each, with the topmost two layers relaxed. The Au(211) surface was modeled with slabs that had a 3 atomic row deep terrace and a 2-atom-wide ((2×3)), 4-atom-wide ((4×3)), or 5-atom-wide ((5×3)) step edge and consisted of 3 layers of Au perpendicular to the terrace. The topmost 4 atomic rows of Au were relaxed. The Au(563) surface was modeled with a slab consisting of 4 layers of Au (in the direction normal to the terrace) for a total of 36 atoms in the unit cell, of which the topmost 14 Au atoms were relaxed. Au atoms that were not relaxed

were held at their bulk positions. The different surface unit cells allow different adsorbate coverages to be modeled. All slabs were sampled on a Γ -centered $5 \times 5 \times 1$ Monkhorst-Pack k-point grid. Neighboring slabs were separated by 20-24 Å of vacuum in the z direction, with dipole decoupling in the z direction.⁴⁵ The total energies of the gas-phase species were calculated in an $18 \times 18.2 \times 18.4$ Å³ simulation cell. To compensate for a systematic error in RPBE, a correction of 0.45 eV was applied to the total energy of the gas-phase CO₂ molecule.⁴⁶ Geometry optimization was considered converged when the residual force in each relaxed degree of freedom fell below 0.03 eV/Å.

The adsorption energy (ΔE_{ads}) of an adsorbate on a blank or functionalized Au slab was calculated as:

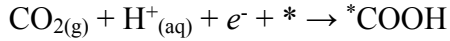
$$\Delta E_{ads} = E_{total} - E_{slab} - E_g$$

where E_{total} , E_{slab} , and E_g are the DFT total energies of the system, the Au slab (blank or functionalized), and the neutral adsorbate species isolated in the gas phase, respectively. Following prior studies,^{47, 48} the adsorption energy of a thiolate molecule in a dithiolate-Au complex was calculated as:

$$\Delta E_{ads} = \frac{1}{2} (E_{total} - E_{slab} - E_{Au}) - E_g$$

where, without loss of generality, E_{Au} is the energy of an Au atom in bulk Au. The DFT-calculated total energy adsorption energies are listed in Table S1. It should be noted that for the thiolates, which do not have appreciable partial pressures in the gas phase in this study, using a gas-phase reference is not intended to reflect their stabilities vs. desorption, but merely to allow the relative stabilities of different surface thiolate states to be estimated, and to facilitate comparison with existing and future theoretical studies for adsorption of similar thiolates on Au and other metals.

According to the computational hydrogen electrode,⁴⁹ the free energy of ($H^+ + e^-$) can be calculated as $G[H^+ + e^-] = \frac{1}{2}G[H_{2(g)}]$ at pH=0 and 0 V vs. SHE. The free energy at a different pH value can be corrected by $+k_B T \cdot \ln[H^+]$, where $[H^+]$ is the concentration of H^+ ions. Thus, for instance, the free energy (ΔG_{rxn}) of CO_2 reduction to COOH via the step,



was calculated as:

$$\Delta G_{rxn}^{SHE} = G[COOH^*] - G[CO_{2(g)}] - G[*] - \left(\frac{1}{2}G[H_{2(g)}] + k_B T \cdot \ln[H^+] \right)$$

Here * indicates an adsorbed species or, by itself, denotes a free site, and henceforth we will use it to denote the surface reaction intermediates, e.g. *H and *COOH, in HER and CO_2RR . Since the RHE is related to the SHE by $U_{RHE} = U_{SHE} + k_B T \cdot \ln[H^+]/e$, the reaction free energy of Step 1 can be re-written as:

$$\Delta G_{rxn}^{RHE} = G[COOH^*] - G[CO_{2(g)}] - G[*] - \frac{1}{2}G[H_{2(g)}]$$

The equilibrium potential for this reaction step is equal to $U^0 = -\Delta G_{rxn}/e$. The source of proton at neutral pH is the dissociation of water prior to the onset of the $2e^-$ reduction of water. The reaction step can alternatively be written by replacing $H^+_{(aq)}$ with $H_2O - OH^-_{(aq)}$, but the results are identical on the RHE.⁵⁰

For the individual terms in the ΔG_{rxn} expressions: The free energies of gas-phase H_2 , CO_2 , and CO were calculated as:⁵¹

$$G_x = E + \Delta G(T, p) = E + \left(E^{ZPE} + \Delta h(T, p^*) - Ts(T, p^*) + k_B T \cdot \ln\left(\frac{p}{p^*}\right) \right)$$

where E and E^{ZPE} are the DFT total energy and zero-point energy (ZPE) of species H_2 or CO_2 , respectively, T is temperature, h and s are the enthalpy and entropy of the gas-phase species, respectively, and p is pressure with $p^\circ = 1$ bar as the reference pressure. Δh is equal to $h(T, p^\circ) - h(0 \text{ K}, p^\circ)$. In this work T and p were set to ambient conditions (298.15 K and 1 bar). The values of the enthalpies and entropies for H_2 , CO_2 , and CO were obtained from the NIST Chemistry WebBook.⁵² Using experimentally measured enthalpies and entropies better accounts for non-ideality than a pure statistical thermodynamics approach, although the differences are likely negligible for these simple gasses. The corresponding E^{ZPE} and ΔG values are listed in Table S1 in Supporting Information.

The free energy of an adsorbate on an Au surface (e.g. *H , *COOH) was calculated as:

$$G_{ads} = E + \Delta G(T) + \Delta E_{solv} + \mu_0 \cdot \varepsilon = E + \left(E^{ZPE} + \Delta u(T) - Ts(T) \right) + \Delta E_{solv} + \mu_0 \cdot \varepsilon$$

where E is the DFT total energy of the system, Δu is the change in internal energy from 0 K to T , ΔE_{solv} is the solvation energy correction, μ_0 is static surface dipole moment at zero electric fields, and ε is the electric field at the surface. E^{ZPE} (as well as E^{ZPE} term in the free energy of gas-phase species above), Δu , and s were calculated from the vibrational frequencies associated with the normal modes of the adsorbed species, which were calculated using two-sided finite difference approximation of the dynamical matrix with a displacement of 0.01 Å. Previously reported values⁴⁶ for *CO and *COOH were used for ΔE_{solv} . The presence of thiolate species was not taken into consideration based on the assumption that their solvation effects were largely canceled out in the calculation of ΔG_{rxn} . The dipole-field term ($\mu_0 \cdot \varepsilon$) is the first-order approximation to the Stark effect, which has been found to be significant for *COOH , a key intermediate in CO_2RR , on Ag ⁵³ although its polarizability is negligible ($|0.2| \text{ eÅ}^2/V$ or less), which justifies the use of the approximation.⁵⁴ See Table S1 for the values of E^{ZPE} , ΔG , ΔE_{solv} ,

and μ_0 for key adsorbed states. In this study, the direction of a dipole moment is consistent with that of the electric field (from positive to negative charges), and a positive dipole is in the positive z direction, which points away from the surface. A representative value of -1.0 V/\AA was used for \mathcal{E} .⁵³

For a co-adsorption system (e.g. $^*\text{COOH}$ with a thiolate species), E , E^{ZPE} , ΔG and μ_0 are those of the overall system, and the reference system (i.e. $G[*]$) refers to Au with the thiolate. The minimum free energy adsorption geometry of a thiolate species on Au was determined from multiple initial configurations, each of which was subjected to a coarse-grain *ab initio* molecular dynamics simulation that thermally annealed it at 300 K, followed by energy minimization. The vibrational and dipole-field contributions to the free energy were considered in identifying minimum free energy structures.

3. Results and discussion

3.1 Electrochemical measurements

We determined the onset potentials for CO_2RR and HER based on Tafel plots⁵⁵ (see Fig. S1 in Supporting Information), which are summarized in Table 1. The only major gas products from the electrolysis (defined as those having a FE > 0.1%) were H_2 and CO on all the Au electrodes. The onset of CO evolution at ca. $-0.3 \text{ V}_{\text{RHE}}$ on blank Au foils is consistent with previous reports⁶ and has been conclusively proven by Dunwell et al. recently with surface enhanced infrared absorption spectroscopy, which captured the vibrational signature of CO on Au under a square-wave potential profile.⁵⁶ The onset potential for CO evolution on both of the functionalized Au electrodes (2-PET-Au and 2-MPA-Au) was shifted to $-0.24 \text{ V}_{\text{RHE}}$, a 90 mV anodic shift

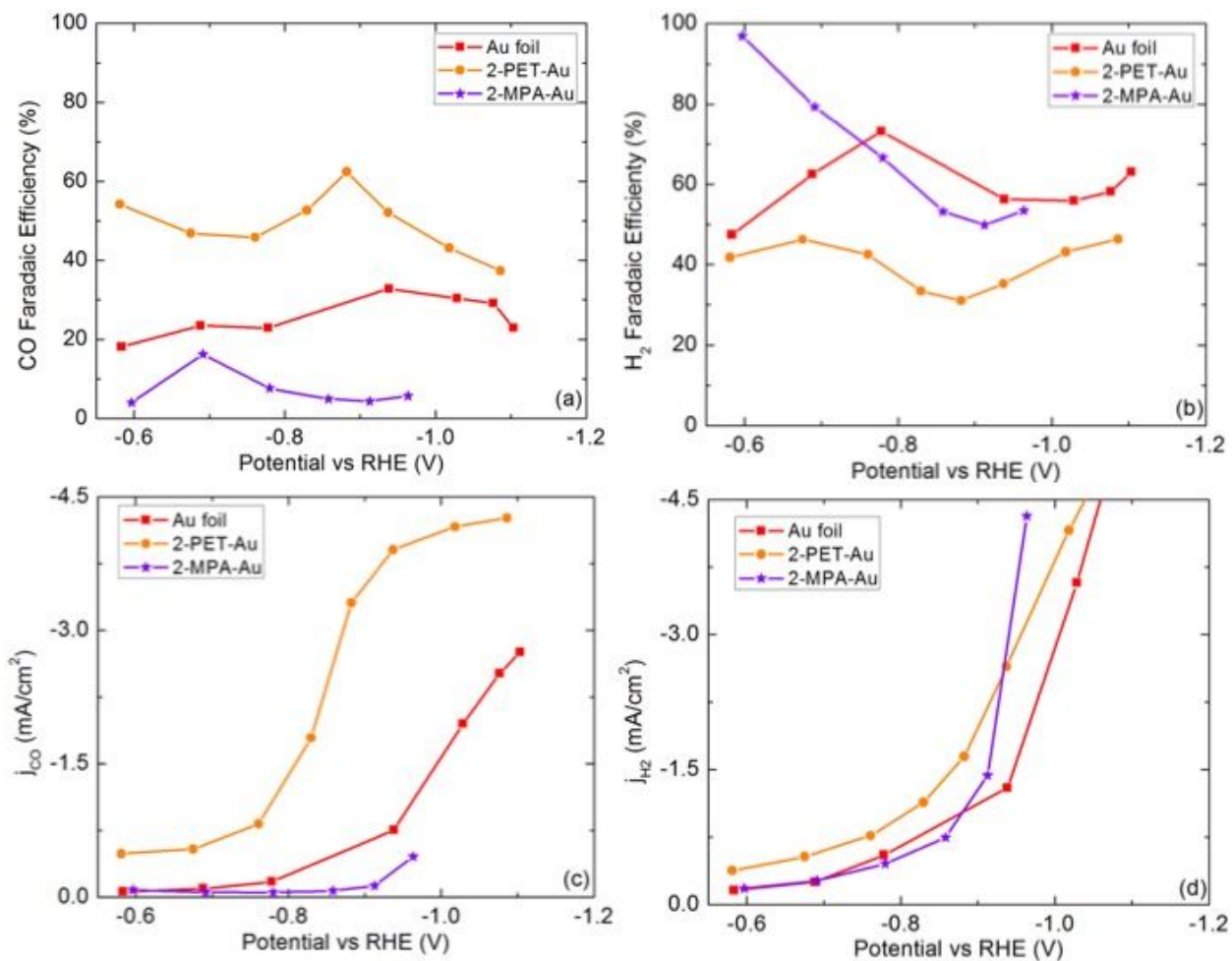
compared to blank Au. For HER, the onset potential barely changed on 2-PET-Au, while a 160 mV anodic shift was observed on 2-MPA-Au.

Table 1 Comparison of onset potentials (in V_{RHE}) of HER and CO_2RR on blank and functionalized Au foil electrodes at room temperature based on the Tafel plots.

Electrode	HER	CO_2RR
blank Au	-0.27	-0.33
2-PET-Au	-0.26	-0.24
2-MPA-Au	-0.11	-0.24

Fig. 3 compares the FE and partial current densities for CO and H_2 (j_{CO} and j_{H_2}) in CO_2 electrolysis on blank Au, 2-PET-Au, and 2-MPA-Au. The total current density (j_{tot}) on blank Au foil was similar to that obtained by Kauffman et al. over bulk Au in 0.1 M KHCO_3 .⁹ In the $-0.6 \sim -0.9 V_{\text{RHE}}$ range, remarkably, the FE of CO was approximately doubled while the FE of H_2 was suppressed by half on 2-PET-Au vs. blank Au. Both j_{CO} and j_{H_2} , and especially j_{CO} , increased (Fig. 3c, 3d) and so did the total current density (Fig. 3e). At $-0.8 V_{\text{RHE}}$, for example, the FE for CO formation on 2-PET-Au was twice that on blank Au, and the current density for CO on 2-PET-Au was 7.6 times that on blank Au. At ca. $-0.9 V_{\text{RHE}}$ the FE and partial current density for CO evolution on 2-PET-Au are comparable to the performance of the anodically modified Au reported by Kuhl et al.⁵⁷ 2-MPA-Au exhibited a different effect on product selectivity: The FE for CO evolution was suppressed while the FE for H_2 was promoted to near unity around $-0.6 V_{\text{RHE}}$. The partial current density for CO was somewhat lower than on blank Au while that for

H₂ was comparable to blank Au down to ca. -0.9 V_{RHE}, beyond which the latter rapidly increased compared to blank Au. These findings reveal no clear sign of thiolate poisoning and passivation of the Au electrodes.



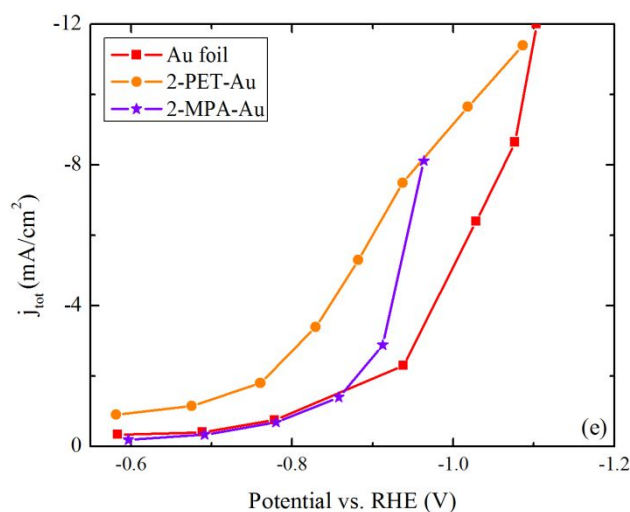


Fig. 3 Comparison of electrolytic behavior of blank and thiol-functionalized Au foil electrodes at room temperature and $p_{\text{CO}_2} = 1$ atm. (a) Faradaic efficiency of CO; (b) Faradaic efficiency of H₂; (c) partial current density of CO (j_{CO}); (d) partial current density of H₂ (j_{H_2}); (e) total current density (j_{tot}), all in CO₂ electrolysis carried out in CO₂-saturated 0.1 M KHCO₃. Note that the y-axis scales are made identical in (c) and (d) to facilitate comparison, which causes some data points to be cut off. For the full version of panel (d) see Fig. S2.

3.2 Stability of the thiols on Au

To verify the stability of 2-PET and 2-MPA on Au, the electrodes were interrogated using *ex situ* ATR-IR before and after they were used in CO₂ electrolysis. The resulting spectra are presented in Fig. 4. On 2-PET-Au, (i) the CH₂ wagging mode in –CH₂–S at 1260 cm⁻¹; (ii) the –CH₂–CH₂– bending mode at 1380 cm⁻¹; (v) the –CH₂– asymmetric stretching mode at 2947 cm⁻¹; and the aromatic ring C=C stretching modes at (iii) 1580 cm⁻¹ and (iv) 1623 cm⁻¹ are detected on the electrode both as prepared and post electrolysis at -1.1 V_{RHE} for 15 minutes (peak assignments as indicated in Fig. 4a).⁵⁸⁻⁶¹ The overall intensities of the signals are similar before and after the

electrolysis. The blue shift of peak (i) to higher wavenumber and the change of relative intensities between the $-\text{CH}_2-\text{CH}_2-$ bending mode (ii) and aromatic ring $\text{C}=\text{C}$ stretching modes (iii and iv) may be attributed to a conformational change in the molecule.⁶²

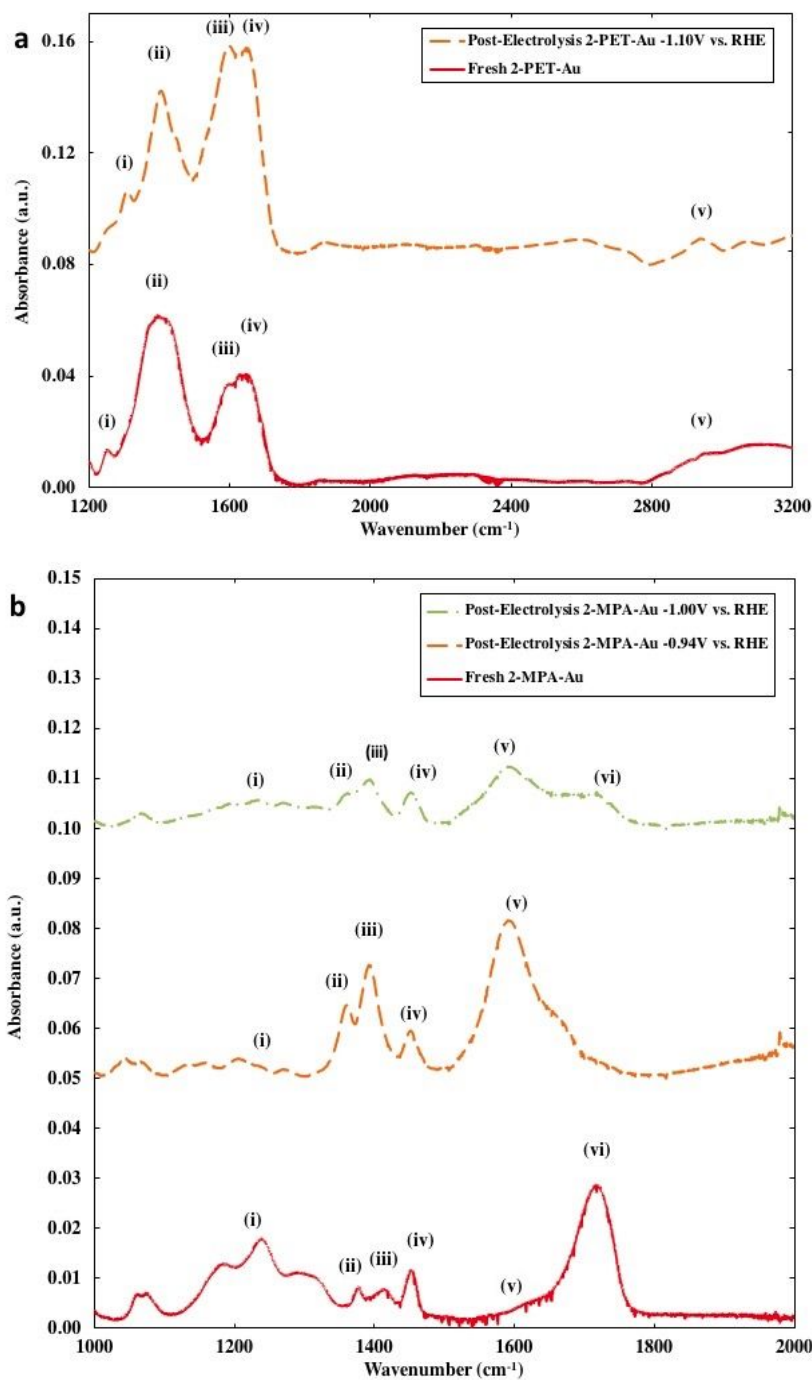


Fig. 4 ATR-IR spectra for as-prepared and post-electrolysis (a) 2-PET-Au and (b) 2-MPA-Au electrodes. The electrolysis was done by holding each functionalized electrode in CO₂-saturated 0.1 M KHCO₃ at each given potential for 15 minutes.

In the spectrum of the as-prepared 2-MPA-Au electrode (Fig. 4b), the peaks at (i) 1241 cm⁻¹, (iv) 1449 cm⁻¹, and (vi) 1723 cm⁻¹ are assigned to C-C stretching,⁶⁰ asymmetric stretching of the -CH₃ group, and C=O stretching of the -COOH group, respectively. After 15 minutes of CO₂ electrolysis at -0.94 V_{RHE}, peak (vi) diminished while a new set of peaks became prominent at (ii) 1372 cm⁻¹, (iii) 1421 cm⁻¹, and (v) 1602 cm⁻¹, which are assigned to various asymmetric and symmetric stretching of the deprotonated -COO group, indicating that the dominant species on the surface changed from the singly deprotonated acid-thiolate form (CH₃CHSCOOH) to the doubly deprotonated carboxylate-thiolate form (CH₃CHSCOO) of 2-MPA. The assignment regarding the deprotonation of the -COOH group is consistent with an expected increase of interfacial pH due to highly negative electrode potentials; with infrared spectra of aqueous-phase acetic acid vs. sodium acetate; and with surface science findings for the interaction of carboxylic acids on metals and oxides.⁶³⁻⁶⁷ Comparison with the literature excludes the possibility that these peaks are due to adsorbed HCO₃⁻ or CO₃²⁻ species.^{56, 68} After 15 minutes of electrolysis at -1.0 V_{RHE}, the intensities of most of the peaks diminished, suggesting notable loss of the ligand molecules.

The reductive desorption of alkanethiols (including carboxylate-containing species such as MPA) and arenethiols has been previously studied.^{27-29, 69} Most of those studies used basic solutions, in which the peak reduction potential fell between -0.7 and -1.1 V_{Ag/AgCl}. The fate of thiol ligands following electrochemical reduction is debated. Jacob et al. studied decanethiol and

octadecanethiol on Au in 0.1 M KOH using sum frequency generation and suggested that large hydrophobic ligands remain close to the electrode even after reductive desorption.⁷⁰ Our ATR-IR experiments present clear evidence for the persistence of chemisorbed 2-PET and 2-MPA on the Au electrodes down to ca. $-0.9 V_{\text{RHE}}$.

In addition, we performed linear sweep voltammetry (LSV) to analyze the thiol coverage before and after CO₂ electrolysis (15 minutes in CO₂-saturated in 0.1 M KHCO₃). The LSV experiments were conducted at a scan rate of 50 mV/s in 0.5 M KOH for 2-PET-Au and 0.1 M KOH for 2-MPA-Au, respectively. Because the reductive desorption peak of 2-PET in 0.1 M KOH was indiscernible, a higher concentration of 0.5 M KOH was used instead. The potential was scanned cathodically from 0 to $-1.5 V_{\text{Ag/AgCl}}$ to reductively desorb surface thiol species, thereby quantifying the amount of the ligands that were present on the freshly prepared samples and on the post CO₂ electrolysis samples.

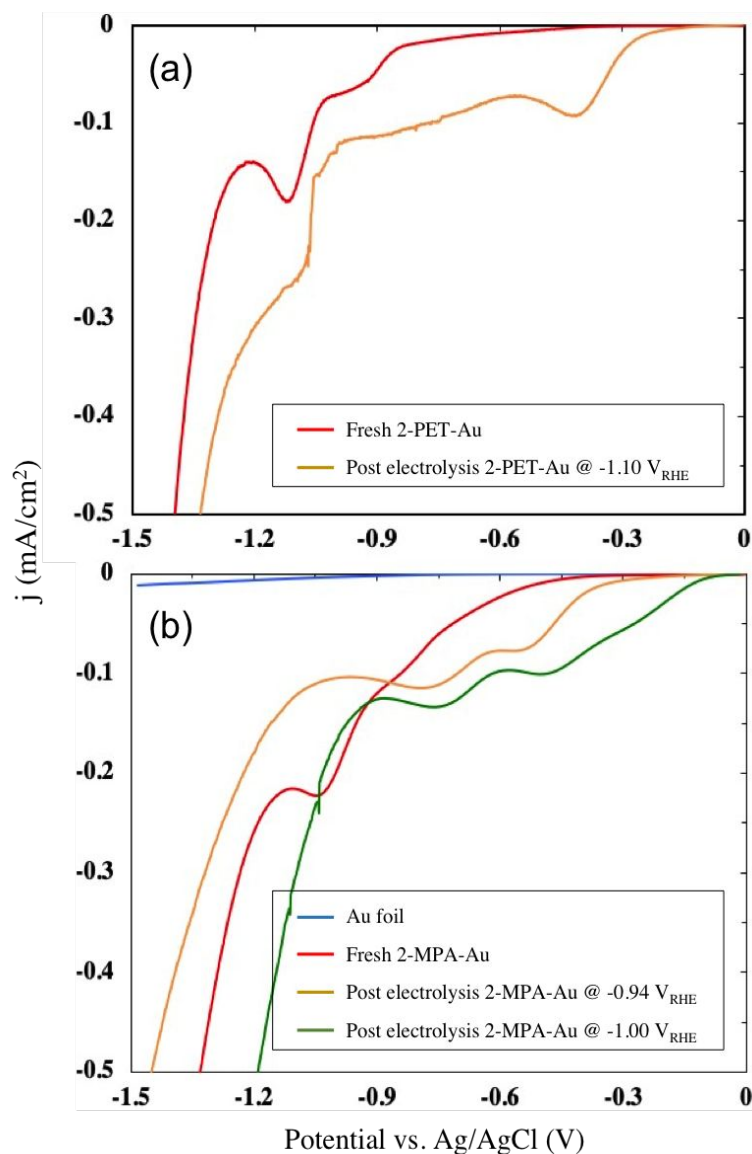


Fig. 5 Linear sweep voltammograms of differently treated (a) 2-PET-Au in 0.5 M KOH, and (b) 2-MPA-Au in 0.1 M KOH, at room temperature. Scan rate was 50 mV/s.

Fig. 5a shows the LSV of 2-PET-Au in 0.5 M KOH aqueous electrolyte. The difference in background current arose from non-Faradaic capacitive charging. The reductive peak at -1.06 V_{Ag/AgCl} is integrated to give an estimated reductive charge of 116 $\mu\text{C}/\text{cm}^2$ for the freshly prepared 2-PET-Au, which corresponds to a coverage of 1.2×10^{-9} mol/cm² (summarized in Table 2), or 0.49 ML based on 1.5×10^{15} surface Au atoms per cm² on Au(111). This value is close to

those reported in the literature.⁷⁰ After 15-minute electrolysis at $-1.1 V_{\text{RHE}}$ in CO_2 -saturated 0.1 M KHCO_3 , $89 \mu\text{C}/\text{cm}^2$ was obtained by integrating the reductive peak corresponding to $9.26 \times 10^{-10} \text{ mol}/\text{cm}^2$, which indicates that 77% of the 2-PET remained on Au surface following CO_2 electrolysis at $-1.1 V_{\text{RHE}}$ for 15 minutes.

Fig. 5b shows the corresponding results of 2-MPA-Au in 0.1 M KOH. The LSVs of the freshly prepared and post-electrolysis (at -0.94 and $-1.00 V_{\text{RHE}}$) 2-MPA-Au were measured. The integrated reductive charges were $95 \mu\text{C}/\text{cm}^2$, $89 \mu\text{C}/\text{cm}^2$, and $63 \mu\text{C}/\text{cm}^2$, respectively. Thus the freshly prepared 2-MPA-Au had a lower surface coverage of thiolates than the freshly prepared 2-PET-Au did, and a greater amount of 2-MPA was lost from the surface than 2-PET through CO_2 electrolysis at a comparable potential, which suggests that 2-PET is bonded to Au more strongly than 2-MPA, in line with our ATR-IR findings. The results of quantitative analysis based on the LSV experiments are summarized in Table 2. A significant percentage of each ligand did persist on Au through CO_2 electrolysis at ca. $-1 V_{\text{RHE}}$, which suggests that the ligands are stable if CO_2 electrolysis was carried out at more modest potentials.

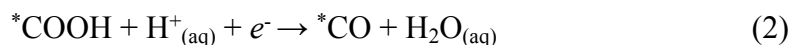
Table 2 Reductive charge and coverages of 2-PET and 2-MPA on Au electrodes estimated from linear sweep voltammetry.

Ligand	Sample	Reductive Charge ($\mu\text{C}/\text{cm}^2$)	Coverage (mol/cm^2)	Percent remain (%)
2-PET	Fresh	116	1.20×10^{-9}	100
	$-1.10 V_{\text{RHE}}$	89	9.26×10^{-10}	77

2-MPA	Fresh	95	9.85×10^{-10}	100
	-0.94 V _{RHE}	89	9.21×10^{-10}	94
	-1.00 V _{RHE}	63	6.56×10^{-10}	72

3.3 Electrochemical activity of blank Au sites

Consistent with the general pattern of under-coordinated Au sites being more catalytically active,⁷¹⁻⁷³ our DFT calculations suggest that the observed electrochemical activity for CO₂RR on blank Au is most consistent with defect sites rather than terrace sites. We use the Au(111), (100), (211), and (563) facets to represent Au sites of different morphologies (hexagonal close-packed and square close-packed terraces, step edges, and corners, respectively), which have different coordination numbers (9, 8, 7, and 6, respectively).⁷⁴ We consider the following steps as representing the main steps in CO₂ reduction (Steps 1, 2, and 3) and H₂ evolution (Step 4):^{46, 75}



We take the thermodynamic approach originally proposed by Nørskov et al. and take the lowest equilibrium potential in the mechanism of a reaction to be the limiting potential for the whole reaction. This approach only takes the intrinsic reactivity of a surface site, not the complex interfacial kinetics, into account, but it has been fruitfully applied by a number of researchers to elucidate the HER and CO₂RR activities of electrocatalysts.^{11, 12, 76} Thus the equilibrium potential of Step 4 is taken to be the limiting potential for H₂ evolution. The thermodynamic barrier represented by the more negative of the equilibrium potentials for Steps 1

and 2 controls the activity of electrochemical CO₂ reduction on Au since the transfer of a proton/electron to an oxygen center generally occurs with a small additional kinetic barrier,^{49, 53} while calculations show that the addition of a hydrogen atom (i.e. a H⁺/e⁻ pair) to *COOH on Au results in the formation and spontaneous detachment of a water molecule. The equilibrium potential for Step 1 is found to be negative while that of Step 2 positive on all four surfaces. CO desorption (Step 3) from bulk Au is not expected to influence the limiting potential for CO₂RR because experimentally it is complete well below 300 K.^{77, 78}

The calculated limiting potentials for HER and CO₂RR on blank Au sites are listed in Table 3 (see Fig. S3 for snapshots and Table S1 for DFT adsorption energies for the *H and *COOH intermediates). The *cis* and *trans* configurations of *COOH are practically isoenergetic *in vacuo* on every Au surface in DFT total energy. The presence of an interfacial electric field, on the other hand, would have a stabilizing effect on the *COOH intermediate via the last term in G_{ads} (i.e. $\mu_0 \cdot \varepsilon$, see the Computational methods section) if *COOH is in the *trans* state, which is what is reported below. This stabilization amounts to -0.25 eV at -1.0 V/Å.⁵³ Fig. 6 shows the calculated reaction free energy diagram for CO₂RR on blank Au(111) and Au(211), and on (2-PETt)₂Au/Au(211), which will be mentioned below.

Table 3 Calculated limiting potentials for HER and CO₂RR and their differences (in V_{RHE}) on blank Au sites.

	surface	HER	CO ₂ RR	diff.
	unit cell			
Au(111)	(3×3)	-0.34	-0.66	-0.32
Au(100)	(3×3)	-0.35	-0.63	-0.28
Au(211)	(4×3)	-0.22	-0.35	-0.13
Au(563)	9 Au/layer	-0.23	-0.26	-0.03

Results are based on minimum free energy configurations for one *H or *COOH per respective surface unit cell. See Fig. S3 for snapshots of the minimum free energy configurations.

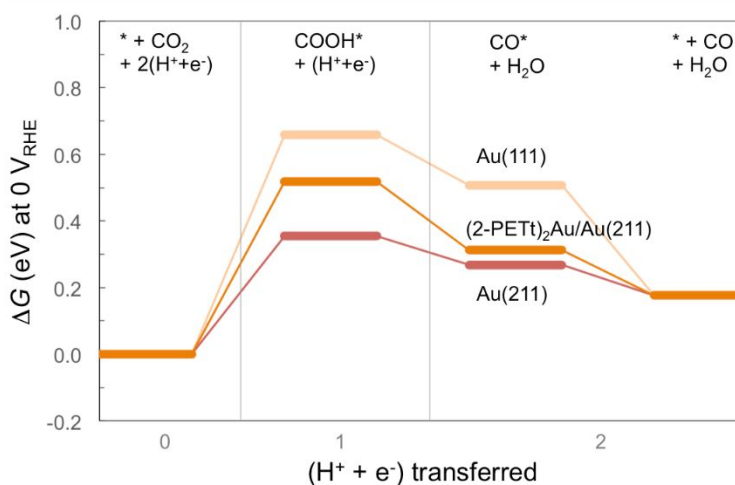


Fig. 6 DFT calculated reaction free energy diagram (ΔG at 0 V_{RHE}) for electrochemical CO₂ reduction on blank Au(111) and Au(211), and on (2-PETt)₂Au/Au(211).

The predicted limiting potentials for CO₂RR on Au(111) and (100) are ca. -0.6 V_{RHE}, whereas those for Au(211) and (563) are ca. -0.3 V_{RHE}, in close agreement with the computational literature on CO₂RR on Au.^{10, 11} The overpotential for CO₂RR on defect Au sites is thus ca. 300 mV smaller than on terrace Au sites, whereas the overpotential for HER varies less, by ca. 100

mV. Thus the *difference* in the overpotential for CO₂RR vs. HER narrows as the coordination of the Au site decreases, although HER remains more active than CO₂RR on all of the blank Au sites considered here.

3.4 Interaction of thiolates with CO₂RR and HER intermediates

Consistent with the proposed reconstruction process (Fig. 2), we take thiolates directly adsorbed on Au(111) as the reservoir of a given thiolate species in the system. It can be seen from Table S1 that open defect sites are significantly more favorable adsorption sites for the RS or (RS)₂Au thiolate states than Au(111), diffusion permitting.^{79, 80} Thus thiolate species adsorbed on defect sites are much more stable than their counterparts on Au(111), and would therefore remain on a polycrystalline Au surface to more negative potentials when subjected to a cathodic scan. We have taken Au(211) as the representative defect site, and minimized the energies of several 2-PET and 2-MPA thiolate states adsorbed thereon, including directly adsorbed thiolates (referred to below as 2-PETt and 2-MPAtt; here 2-MPAtt refers to the doubly deprotonated form) and dithiolate-Au complexes (referred to below as (2-PETt)₂Au and (2-MPAtt)₂Au) (Fig. 7). Each thiolate state is considered at two different edge coverages (θ , defined to be the ratio of the number of Au edge atoms occupied by a thiolate (directly bonded to any part of it) to the total number of Au edge atoms in a unit cell; see Table 4). The dithiolate-Au complexes are aligned with the step edge, with the Au adatom located on a top site and each S atom linking the Au adatom to a neighboring Au atom, whereas directly adsorbed 2-PETt and 2-MPAtt bond preferentially through the S atom on a bridge site.

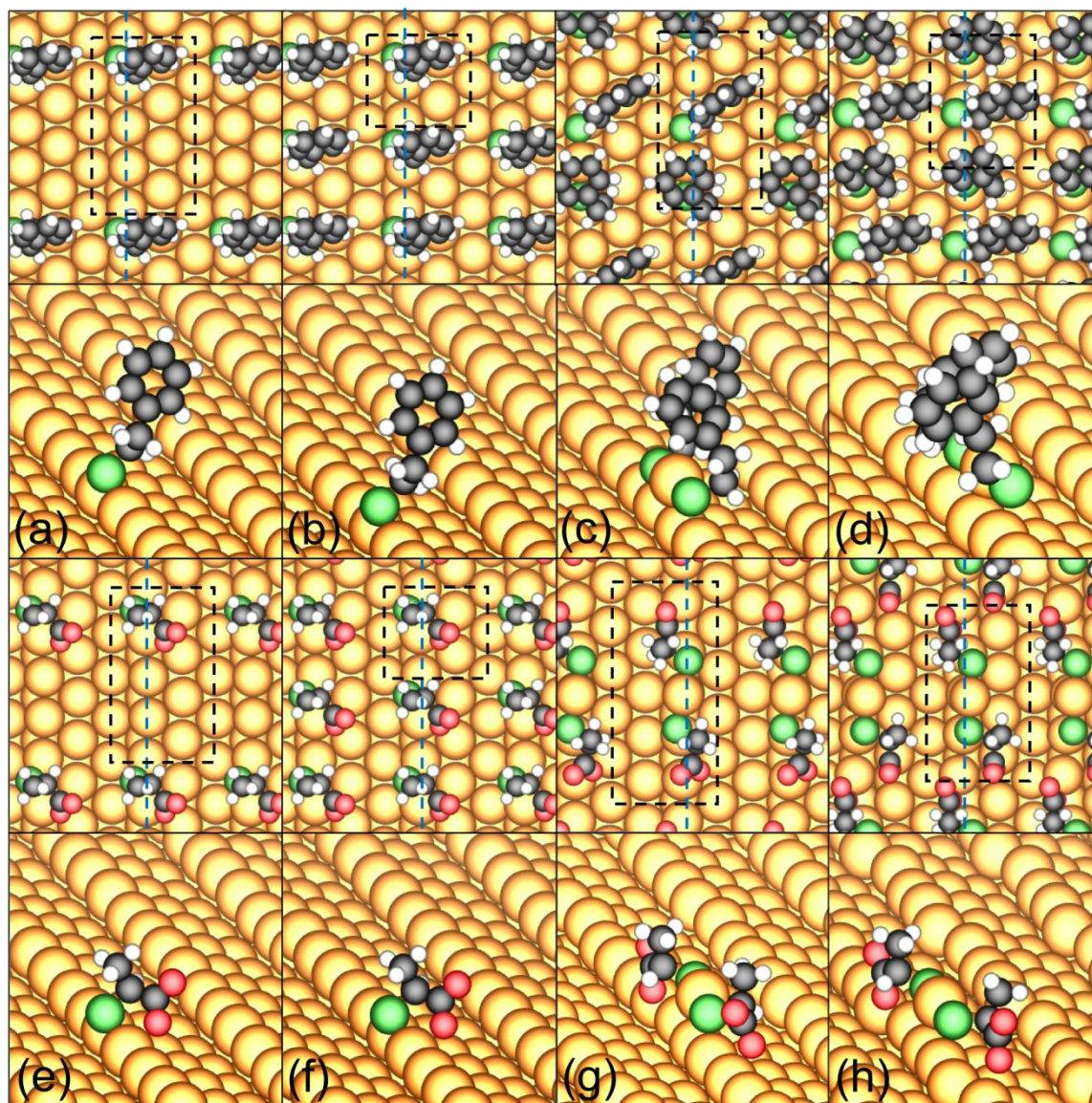


Fig. 7 Top (top panels) and tilted side (bottom panels) views of DFT-calculated minimum free energy geometries for (a, b) 2-PETt on (4×3) and (2×3) unit cells; (c, d) (2-PETt)₂Au on (4×3) and (3×3) unit cells; (e, f) 2-MPAtt on (4×3) and (2×3) unit cells; (g, h) (2-MPAtt)₂Au on (5×3) and (4×3) unit cells, on step edge of Au(211). Yellow, green, red, black, and white spheres represent Au, S, O, C, and H atoms, respectively. Green and black dashed lines in top views indicate step edge and surface unit cells, respectively. For clarity, periodic images of adsorbates have been removed from the side views.

Table 4 Calculated limiting potentials for HER and CO₂RR and their differences (in V_{RHE}) on thiolate-functionalized Au(211) step edge, size of surface unit cell used in modeling, edge coverage (θ), chemical potential of thiolate (μ , in eV/RS), numbers of RS units and Au edge atoms per unit cell (n_{RS} , n_{Au}) used in computing the average edge free energy, and the Boltzmann distribution (P , in %, calculated at $T=298.15$ K and $\varepsilon=-1.0$ V/Å) for the various thiolate states on Au(211).

	HER	CO ₂ RR	diff.	surface unit cell	θ	μ	n_{RS} , n_{Au}	P
2-PETt/Au(211)	-0.31	-0.50	-0.19	(4×3)	2/4	-0.59	1, 4	0
	-0.70	-1.80	-1.10	(2×3)	1	-0.54	1, 2	39
(2-PETt) ₂ Au/Au(211)	-0.40	-0.52	-0.12	(4×3)	3/4	-0.55	2, 4	43
	-0.63	-1.21	-0.58	(3×3)	1	-0.38	2, 3	18
2-MPAtt/Au(211)	-0.27	-0.65	-0.38	(4×3)	2/4	-0.71	1, 4	1
	-0.75	-1.92	-1.17	(2×3)	1	-0.47	1, 2	14
(2-MPAtt) ₂ Au/Au(211)	-0.62	-0.92	-0.30	(5×3)	4/5	-0.78	2, 5	18
	-0.69	-	-	(4×3)	1	-0.66	2, 4	67

Results are based on minimum free energy configurations for one thiolate species and one *H or *COOH per respective surface unit cell. See Fig. S4 for snapshots of the minimum free energy geometries of *H and *COOH co-adsorbed with these thiolate species. Values in bold are limiting potentials more positive than or equal to the corresponding values on blank Au(111) in Table 3. “-” indicates no stable *COOH is obtained.

The calculated limiting potentials of HER and CO₂RR *in the presence of the thiolates* are summarized in Table 4. Cathodic shifts vs. blank Au(211) is observed in all cases, which we attribute to the destabilization of the key intermediates, *H and *COOH, by the thiolates. At $\theta = 1$ the directly adsorbed 2-PETt significantly lowers the limiting potential for CO₂RR to well below -1.0 V_{RHE}. This is due to the poisoning effect of S through surface-mediated Pauli

repulsion and covalent interactions,⁸¹⁻⁸³ and a lack of available Au edge atoms to the top of which *COOH preferentially bonds. At a lower edge coverage (e.g. $\theta = 2/4$) free Au edge atoms are available where the limiting potentials are closer to those on blank Au(211). On the other hand, short of fully occupying the step edge ($\theta = 1$), the dithiolate complex (2-PETt)₂Au has only a mild impact on the limiting potential of CO₂RR, with a small cathodic shift of 170 mV compared to blank Au(211) at $\theta = 3/4$. The effect on HER follows a similar pattern. Table 4 shows that 2-MPAtt states tend to have a more cathodic impact on HER and CO₂RR than 2-PETt states do at comparable edge coverage (see Fig. S5 for illustration of the trend). This is because the –COO group is bonded to the surface and creates additional repulsion for nearby *H or *COOH at higher coverage.

The few limiting potentials that are more anodic than the corresponding values on blank Au(111) are indicated in bold in Table 4. Also listed are the Boltzmann probabilities of the different thiolate states based on their average edge free energies ($P_i \propto e^{-\frac{\bar{g}_i}{kT}}$), which suggest that edge sites should be densely occupied by various thiolate states. The average edge free energy (\bar{g} , in eV/Au) is calculated using quantities listed in Table S1, as:

$$\mu(T, \varepsilon) = \left(\Delta E_{ads}^{211} + \Delta G(T)^{211} + \mu_0^{211} \cdot \varepsilon \right) - \left(\Delta E_{ads}^{111} + \Delta G(T)^{111} + \mu_0^{111} \cdot \varepsilon \right)$$

$$\bar{g}(T, \varepsilon) = \frac{n_{RS}}{n_{Au}} \mu$$

where μ is the chemical potential of a RS group in an edge state relative to RS directly adsorbed on Au(111), n_{RS} and n_{Au} are total numbers of RS units and Au edge atoms per unit cell, and ΔE_{ads} and $\Delta G(T)$ as defined in Methods. The only thiolate state that occurs favorably at high edge coverage and also promotes CO₂RR compared to blank Au(111) is (2-PETt)₂Au (at $\theta = 3/4$).

The *activity* of Au sites for CO₂RR thus follows this order: blank defect sites ($\sim -0.3 V_{\text{RHE}}$) > defect sites with 2-PETt ($\sim -0.5 V_{\text{RHE}}$) > blank terrace sites ($\sim -0.6 V_{\text{RHE}}$) > defect sites with 2-MPAtt ($\sim -0.9 V_{\text{RHE}}$). Since the reconstruction-induced (2-PETt)₂Au/defect sites are more active than the original blank terrace sites for CO₂RR (while being comparably active for HER), one may expect 2-PET to have mild or no poisoning effect on CO₂RR. This is consistent with the observations that j_{CO} was in fact higher than blank Au following 2-PET thiol adsorption but was suppressed on 2-MPA-Au, at $-0.6 V_{\text{RHE}}$ and below (Fig. 2c-2e). Higher adsorption coverage of 2-PET than 2-MPA in the thiol solution treatment (evidenced by Table 2), and different abilities of 2-PET and 2-MPA to reconstruct Au, may contribute to the higher total activity of 2-PET-Au than 2-MPA-Au.

We propose that 2-PET promotes CO₂RR better than 2-MPA does for two reasons: 1) The 2-PET thiolate states set up negative dipole moments (see Table S1), which couples to and stabilizes the positive dipole moment of a nearby *COOH, whereas the 2-MPA thiolate states do the opposite; 2) the 2-PET thiolate states are spatially bulkier at the far end of the molecule away from the surface, whereas the 2-MPA thiolate states have a larger footprint on the surface, creating repulsion for *H or *COOH adsorbed nearby. The situation is not the same as thiolated Au nanoclusters where exterior Au atoms are fully coordinated to thiolate ligands and are therefore inactive toward CO₂RR until de-ligation occurs.^{76, 84, 85} De-ligation exposing reconstructed, active Au sites undoubtedly also occurs in our systems when the thiolates begin to desorb at more negative potentials. This may explain the rapid rise in total current density below ca. $-0.9 V_{\text{RHE}}$ for 2-MPA-Au (cf. Fig. 3e).

We surmise that additional interfacial effects beyond surface reactivity contribute to the improved *selectivity* for CO₂RR (on 2-PET-Au) and for HER (on 2-MPA-Au) vs. blank Au. For

instance, the carboxylate group in 2-MPA may have water/proton conduction properties similar to Nafion that enhance proton concentrations near the electrode, whereas the hydrophobicity of the phenyl group in 2-PET would result in lower interfacial proton concentrations. The interfacial proton activity would further modulate the selectivity of the electrochemical reactions.⁸⁶⁻⁸⁸

4. Conclusions

Thiol ligands containing no nitrogen-based heterocycle, introduced by simply pretreating polycrystalline Au with ethanolic solutions of thiols, have been demonstrated to clearly alter the activity and selectivity of Au for electrochemical CO₂ reduction. Between ca. -0.6 and -0.9 V_{RHE}, up to a 2-fold enhancement in both Faradaic efficiency and current density for CO evolution accompanied by the suppression of the competing H₂ evolution reaction is observed on Au electrodes functionalized with 2-phenylethanethiol (2-PET-Au). On the other hand, functionalization with 2-mercaptopropionic acid (2-MPA-Au) strongly favors H₂ evolution over CO evolution. The total current density is either comparable to (on 2-MPA-Au), or markedly higher than (on 2-PET-Au), that on blank Au. ATR-IR indicates the persistence of chemisorbed 2-PET and 2-MPA on the Au electrodes down to ca. -0.9 V_{RHE}.

We propose that the thiols modify Au by inducing reconstruction of Au surfaces that converts terrace sites into defect sites, which are preferentially occupied by the thiolates of 2-PET and 2-MPA in various states. Among them, the dithiolate-Au complex (2-PETt)₂Au is distinct in having only a mild impact on the catalytic activity of defect sites for CO₂RR. This means that 2-PET induces an increase in the surface density of sites that are also moderately active for CO₂RR, which is consistent with the experimental observations.

Thus, within the range of electrode potential where it is stable on Au, a suitable thiol ligand can create electrochemically active sites on polycrystalline Au electrodes *in situ*, contrary to the conventional expectation that sulfur compounds such as thiols are strong catalyst poisons and should passivate Au electrodes. While various specially prepared Au nanostructures have been reported to exhibit improved performance for CO₂RR compared to polycrystalline Au,^{9, 10,89} our work demonstrates a simple and tunable method based on ligand chemistry to modify the activity and selectivity of Au for electrochemical reactions.

Conflicts of interest

There are no conflicts to declare.

Acknowledgements

This research was supported by the U.S. National Science Foundation under Grant #CBET-1438385 and used high performance computational resources provided the Louisiana State University (<http://hpc.lsu.edu>) and by the National Energy Research Scientific Computing Center, which is supported by the Office of Science of the U.S. Department of Energy under contract #DE-AC02-05CH11231. X.C. acknowledges a Materials Science and Engineering Graduate Assistantship provided by Louisiana State University.

References

1. S. Back, H. Kim and Y. Jung, *ACS Catal.*, 2015, **5**, 965-971.
2. J. Heo, C. R. Staples and P. W. Ludden, *Biochemistry*, 2001, **40**, 7604-7611.
3. J.-H. Jeoung and H. Dobbek, *Science*, 2007, **318**, 1461.
4. H. Dobbek, L. Gremer, O. Meyer and R. Huber, *Proc. Natl. Acad. Sci.*, 1999, **96**, 8884.
5. Y. Hori, K. Kikuchi and S. Suzuki, *Chem. Lett.*, 1985, **14**, 1695-1698.
6. Y. Hori, in *Modern Aspects of Electrochemistry*, eds. C. Vayenas, R. White and M. Gamboa-Aldeco, Springer New York, 2008, vol. 42, ch. 3, pp. 89-189.
7. Y. Hori, A. Murata, K. Kikuchi and S. Suzuki, *J. Chem. Soc., Chem. Commun.*, 1987, 728-729.
8. H. Noda, S. Ikeda, A. Yamamoto, H. Einaga and K. Ito, *Bull. Chem. Soc. Jpn.*, 1995, **68**, 1889-1895.
9. D. R. Kauffman, D. Alfonso, C. Matranga, H. Qian and R. Jin, *J. Am. Chem. Soc.*, 2012, **134**, 10237-10243.
10. W. Zhu, R. Michalsky, Ö. Metin, H. Lv, S. Guo, C. J. Wright, X. Sun, A. A. Peterson and S. Sun, *J. Am. Chem. Soc.*, 2013, **135**, 16833-16836.
11. W. Zhu, Y.-J. Zhang, H. Zhang, H. Lv, Q. Li, R. Michalsky, A. A. Peterson and S. Sun, *J. Am. Chem. Soc.*, 2014, **136**, 16132-16135.

12. H. Mistry, R. Reske, Z. Zeng, Z.-J. Zhao, J. Greeley, P. Strasser and B. R. Cuenya, *J. Am. Chem. Soc.*, 2014, **136**, 16473-16476.
13. J. Christophe, T. Doneux and C. Buess-Herman, *Electrocatalysis*, 2012, **3**, 139-146.
14. M. Watanabe, M. Shibata, A. Kato, M. Azuma and T. Sakata, *J. Electrochem. Soc.*, 1991, **138**, 3382-3389.
15. G. Seshadri, C. Lin and A. B. Bocarsly, *J. Electroanal. Chem.*, 1994, **372**, 145-150.
16. E. Barton Cole, M. Baruch, R. L'Esperance, M. Kelly, P. Lakkaraju, E. Zeitler and A. Bocarsly, *Top. Catal.*, 2015, **58**, 15-22.
17. E. Barton Cole, P. S. Lakkaraju, D. M. Rampulla, A. J. Morris, E. Abelev and A. B. Bocarsly, *J. Am. Chem. Soc.*, 2010, **132**, 11539-11551.
18. J. Hawecker, J.-M. Lehn and R. Ziessel, *J. Chem. Soc., Chem. Commun.*, 1984, 328-330.
19. D. Xiang, D. Magana and R. B. Dyer, *J. Am. Chem. Soc.*, 2014, **136**, 14007-14010.
20. P. Maksymovych, O. Voznyy, D. B. Dougherty, D. C. Sorescu and J. T. Yates, *Prog. Surf. Sci.*, 2010, **85**, 206-240.
21. S. T. Marshall, M. O'Brien, B. Oetter, A. Corpuz, R. M. Richards, D. K. Schwartz and J. W. Medlin, *Nat. Mater.*, 2010, **9**, 853.
22. G. Yang and G.-y. Liu, *J. Phys. Chem. B*, 2003, **107**, 8746-8759.
23. Y. W. Yang and L. J. Fan, *Langmuir*, 2002, **18**, 1157-1164.
24. M.-C. Bourg, A. Badia and R. B. Lennox, *J. Phys. Chem. B*, 2000, **104**, 6562-6567.

25. P. G. Lustemberg, M. L. Martiarena, A. E. Martínez and H. F. Busnengo, *Langmuir*, 2008, **24**, 3274-3279.
26. F. Tielens and E. Santos, *J. Phys. Chem. C*, 2010, **114**, 9444-9452.
27. J. Zhang, Chi and J. Ulstrup, *Langmuir*, 2006, **22**, 6203-6213.
28. K. Uosaki, *Chem. Rec.*, 2009, **9**, 199-209.
29. Y.-T. Tao, C.-C. Wu, J.-Y. Eu, W.-L. Lin, K.-C. Wu and C.-h. Chen, *Langmuir*, 1997, **13**, 4018-4023.
30. J. Noh, E. Ito and M. Hara, *J. Colloid Interf. Sci.*, 2010, **342**, 513-517.
31. D. Hobara, K. Miyake, S.-I. Imabayashi, K. Niki and T. Kakiuchi, *Langmuir*, 1998, **14**, 3590-3596.
32. O. Azzaroni, M. E. Vela, H. Martin, A. Hernández Creus, G. Andreasen and R. C. Salvarezza, *Langmuir*, 2001, **17**, 6647-6654.
33. M. Petri, D. M. Kolb, U. Memmert and H. Meyer, *Electrochim. Acta*, 2003, **49**, 175-182.
34. Y. Kitagawa, D. Hobara, M. Yamamoto and T. Kakiuchi, *J. Solid State Electr.*, 2008, **12**, 461-469.
35. T. Sawaguchi, Y. Sato and F. Mizutani, *Phys. Chem. Chem. Phys.*, 2001, **3**, 3399-3404.
36. M. J. Giz, B. Duong and N. J. Tao, *J. Electroanal. Chem.*, 1999, **465**, 72-79.
37. T. Sawaguchi, Y. Sato and F. Mizutani, *J. Electroanal. Chem.*, 2001, **507**, 256-262.

38. N. A. Kautz and S. A. Kandel, *J. Am. Chem. Soc.*, 2008, **130**, 6908-6909.
39. G. E. Poirier, *Chem. Rev.*, 1997, **97**, 1117-1128.
40. D. C. Sheppard, G. S. Parkinson, A. Hentz, A. J. Window, P. D. Quinn, D. P. Woodruff, P. Bailey and T. C. Q. Noakes, *Surf. Sci.*, 2011, **605**, 138-145.
41. B. Hammer, L. B. Hansen and J. K. Nørskov, *Phys. Rev. B*, 1999, **59**, 7413-7421.
42. G. Kresse and J. Furthmüller, *Phys. Rev. B*, 1996, **54**, 11169-11186.
43. G. Kresse and D. Joubert, *Phys. Rev. B*, 1999, **59**, 1758-1775.
44. N. W. Ashcroft and N. Mermin, *Solid State Physics*, Saunders: College, Orlando, FL, 1976.
45. J. Neugebauer and M. Scheffler, *Phys. Rev. B*, 1992, **46**, 16067-16080.
46. H. A. Hansen, J. B. Varley, A. A. Peterson and J. K. Nørskov, *J. Phys. Chem. Lett.*, 2013, **4**, 388-392.
47. R. Mazzarello, A. Cossaro, A. Verdini, R. Rousseau, L. Casalis, M. F. Danisman, L. Floreano, S. Scandolo, A. Morgante and G. Scoles, *Phys. Rev. Lett.*, 2007, **98**, 016102.
48. G. Hu, R. Jin and D.-e. Jiang, *Nanoscale*, 2016, **8**, 20103-20110.
49. J. K. Nørskov, J. Rossmeisl, A. Logadottir, L. Lindqvist, J. R. Kitchin, T. Bligaard and H. Jónsson, *J. Phys. Chem. B*, 2004, **108**, 17886-17892.
50. J. Rosen, G. S. Hutchings, Q. Lu, S. Rivera, Y. Zhou, D. G. Vlachos and F. Jiao, *ACS Catal.*, 2015, **5**, 4293-4299.

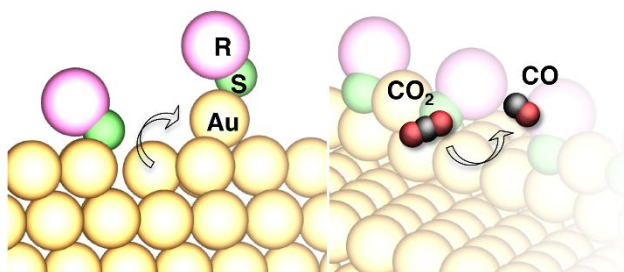
51. M. V. Bollinger, K. W. Jacobsen and J. K. Nørskov, *Phys. Rev. B*, 2003, **67**, 085410.
52. P. J. Linstrom, *National Institute of Standards and Technology*, 2017.
53. L. D. Chen, M. Urushihara, K. Chan and J. K. Nørskov, *ACS Catal.*, 2016, **6**, 7133-7139.
54. S. H. Rawal, W. C. McKee and Y. Xu, *Phys. Chem. Chem. Phys.*, 2017, **19**, 32626-32635.
55. Y. Yan, X. Ge, Z. Liu, J.-Y. Wang, J.-M. Lee and X. Wang, *Nanoscale*, 2013, **5**, 7768-7771.
56. M. Dunwell, Q. Lu, J. M. Heyes, J. Rosen, J. G. Chen, Y. Yan, F. Jiao and B. Xu, *J. Am. Chem. Soc.*, 2017, **139**, 3774-3783.
57. K. P. Kuhl, T. Hatsukade, E. R. Cave, D. N. Abram, J. Kibsgaard and T. F. Jaramillo, *J. Am. Chem. Soc.*, 2014, **136**, 14107-14113.
58. M. Farrag, M. Tschurl, A. Dass and U. Heiz, *Phys. Chem. Chem. Phys.*, 2013, **15**, 12539-12542.
59. H. M. Badawi, *Spectrochim. Acta A*, 2011, **82**, 63-68.
60. G. Socrates, *Infrared and Raman characteristic group frequencies: Tables and charts*, John Wiley & Sons, 2004.
61. C. M. Whelan, M. R. Smyth and C. J. Barnes, *Langmuir*, 1999, **15**, 116-126.
62. G. M. Marshall, F. Bensebaa and J. J. Dubowski, *J. Appl. Phys.*, 2009, **105**, 094310.
63. C. J. Houtman, N. F. Brown and M. A. Barteau, *J. Catal.*, 1994, **145**, 37-53.

64. A. R. Garcia, J. L. da Silva and L. M. Ilharco, *Surf. Sci.*, 1998, **415**, 183-193.
65. W. S. Sim, P. Gardner and D. A. King, *J. Phys. Chem.*, 1996, **100**, 12509-12516.
66. W. O. Gordon, Y. Xu, D. R. Mullins and S. H. Overbury, *Phys. Chem. Chem. Phys.*, 2009, **11**, 11171-11183.
67. F. C. Calaza, T.-L. Chen, D. R. Mullins, Y. Xu and S. H. Overbury, *Catal. Today*, 2015, **253**, 65-76.
68. K. Arihara, F. Kitamura, T. Ohsaka and K. Tokuda, *J. Electroanal. Chem.*, 2001, **510**, 128-135.
69. I. Shin-ichiro, I. Minehiko, H. Daisuke, F. Zhi Qiang, N. Katsumi and K. Takashi, *J. Electroanal. Chem.*, 1997, **428**, 33-38.
70. J. D. C. Jacob, T. R. Lee and S. Baldelli, *J. Phys. Chem. C*, 2014, **118**, 29126-29134.
71. N. Lopez, T. V. W. Janssens, B. S. Clausen, Y. Xu, M. Mavrikakis, T. Bligaard and J. K. Nørskov, *J. Catal.*, 2004, **223**, 232-235.
72. R. Meyer, C. Lemire, S. K. Shaikhutdinov and H. J. Freund, *Gold Bull.*, 2004, **37**, 72-124.
73. S. A. C. Carabineiro and B. E. Nieuwenhuys, *Gold Bull.*, 2009, **42**, 288-301.
74. Z. Zeng and J. Greeley, *Catal. Commun.*, 2014, **52**, 78-83.
75. H. Shin, Y. Ha and H. Kim, *J. Phys. Chem. Lett*, 2016, **7**, 4124-4129.
76. N. Austin, S. Zhao, J. R. McKone, R. Jin and G. Mpourmpakis, *Catal. Sci. Technol.*, 2018, **8**, 3795-3805.

77. S. K. Shaikhutdinov, R. Meyer, M. Naschitzki, M. Bäumer and H.-J. Freund, *Catal. Lett.*, 2003, **86**, 211-219.
78. W. C. McKee, M. C. Patterson, D. Huang, J. R. Frick, R. L. Kurtz, P. T. Sprunger, L. Liu and Y. Xu, *J. Phys. Chem. C*, 2016, **120**, 10909-10918.
79. Y. Santiago-Rodríguez, J. A. Herron, M. C. Curet-Arana and M. Mavrikakis, *Surf. Sci.*, 2014, **627**, 57-69.
80. D.-e. Jiang and S. Dai, *J. Phys. Chem. C*, 2009, **113**, 3763-3766.
81. P. Forzatti and L. Lietti, *Catal. Today*, 1999, **52**, 165-181.
82. J. J. Mortensen, B. Hammer and J. K. Nørskovi, *Surf. Sci.*, 1998, **414**, 315-329.
83. F. Abild-Pedersen, O. Lytken, J. Engbæk, G. Nielsen, I. Chorkendorff and J. K. Nørskov, *Surf. Sci.*, 2005, **590**, 127-137.
84. D. R. Alfonso, D. Kauffman and C. Matranga, *J. Chem. Phys.*, 2016, **144**, 184705.
85. S. Zhao, N. Austin, M. Li, Y. Song, S. D. House, S. Bernhard, J. C. Yang, G. Mpourmpakis and R. Jin, *ACS Catal.*, 2018, **8**, 4996-5001.
86. C. J. Barile, E. C. M. Tse, Y. Li, T. B. Sobyra, S. C. Zimmerman, A. Hosseini and A. A. Gewirth, *Nat. Mater.*, 2014, **13**, 619.
87. J. Wu, F. G. Risalvato, P. P. Sharma, P. J. Pellechia, F.-S. Ke and X.-D. Zhou, *J. Electrochem. Soc.*, 2013, **160**, F953-F957.
88. Z. Peng, Y. Chen, P. G. Bruce and Y. Xu, *Angew. Chem., Int. Ed.*, 2015, **54**, 8165-8168.

89. Z. Cao, D. Kim, D. Hong, Y. Yu, J. Xu, S. Lin, X. Wen, E. M. Nichols, K. Jeong, J. A. Reimer, P. Yang and C. J. Chang, *J. Am. Chem. Soc.*, 2016, **138**, 8120-8125.

Graphical abstract



Simple modification of polycrystalline Au by an appropriate thiol can selectively enhance electrochemical CO₂RR at the expense of HER.